Journal of Ovonic Research Vol. 16, No. 5, September - October 2020, p. 323 - 335

ESTIMATION OF CRYSTALLITE SIZE, LATTICE PARAMETER, INTERNAL STRAIN AND CRYSTAL IMPURIFICATION OF NANOCRYSTALLINE $Al_3Ni_{20}B_x$ ALLOY BY WILLIAMSON-HALL METHOD

A. A. SAAD AKL[a,b,*], M. ELHADI [b,c]
[a]Physics Department, Faculty of Science, Minia University, Minia 11951, Egypt
[b]Physics department, Faculty of Science and humanities, Ed Dawadmi, Shaqra University, Saudi Arabia
[c]Physics Department, Faculty of Science, AlNeelain University, Sudan

$Al_3Ni_{20}B_x$ alloys ($0.06 \leq x \leq 0.12$) nanocrystalline, AlNiB-NCys were synthesized by rapid solidification method in an arc-melt furnace or in an induction furnace. The effect of changing the addition ratio of boron on the crystallography, microstrural, crystal impurifications has been investigated for the $Al_3Ni_{20}B_x$ ternary. The crystal structure of samples obtained using X-ray diffraction was examined. XRD analysis revealed that prepared samples have the polycrystalline nanometric face centered cubic structure. XRD-Line profile analysis by Lorentzian and Gaussian distributions were used to study the microstructure and crystal imperfections of $Al_3Ni_{20}B_x$. Crystallite size and microstrain were estimated using Williamson-Hall plots for the major eight XRD peaks. The data obtained shows that when the metal content is increased, the lattice parameters and volume of unit cell are increased linearly with boron concentration increase. This behavior is believed to be associated with an increase in content B by up to 11% that is entered into the unit cell of the $Al_3Ni_{20}B_x$ system.

(Received May 14, 2020; Accepted October 15, 2020)

Keywords: Crystallite size, Internal strain, Crystal impurification, $Al_3Ni_{20}B_x$ alloys, Williamson-Hall method

1. Introduction

The structural properties of the binary aluminides Al-Ni have been extensively studied by various groups using various techniques [1,2], there are major five stable compounds which crystallize for the binary Al-Ni binary phase. A closer look at these structures shows that the arrangement of Al and Ni is such that there are vacant crystallographic sites. A good example is the structure of the cubic AlNi [space group Pm3m (#221), Ni at (0,0,0) and Al at (½, ½, ½)], wherein the *3c* face-centered site is empty. It is then interesting to see whether this site can be occupied by another atom without modifying the basic structure. Judging from the ionic sizes of Table 1, it is evident that B is an excellent candidate.

Table 1*. Atomic radii and the calculated bond length that may form. The fact that the lattice parameter of the simple cubic-type Al-Ni structure (a=~ 2.888 Å) is equal to the Al-Al bond-length highlights the importance of the Al packing pattern in shaping the crystal structure of these aluminides.*

r_{Al} (Å)	r_{Ni} (Å)	r_B (Å)	Al-Al (Å)	Al-B-Al (Å)	Ni-Ni (Å)	Ni-B-Ni (Å)	Ni-Al-Ni (Å)
1.432	1.246	0.796	2.864	4.454	2.492	4.082	5.356

The addition of B (or defects such as vacancies or antisite atoms) to the stable Al-Ni binary compounds or the variation of the B content across the homogeneity range of the above-

---

[*] Corresponding author: alaaakl2010@windowslive.com

mentioned ternary compounds would lead to noticeable modifications in their physical properties. It is then interesting to investigate how these modifications are correlated with the B content across the ternary Al-Ni-B phase diagram. There is a vast body of literature on the physical (in particular, the mechanical) properties of B micro alloyed (less than one atomic percent) aluminides [3].

Several studies have shown that Al-Ni-B alloys are widely used in many modern applications [1,4,5]. Although the microstructural parameters (lattice parameters, crystallite size, microstrain and residual internal stress) and crystal defects greatly affect the physical properties of materials, especially those of the nanostructures. X-ray diffraction (XRD) is one of the most important tools for studying these parameters. Here, X-rays are diffracted when passing through the internal distances between crystal atoms or crystalline planes. Therefore, the authors dedicated this manuscript to study these serious topics. In this paper, authors used X-ray diffraction, XRD to study the effect of B-contents on the crystalline and microstructure parameters, as well as crystal defects of $Al_3Ni_{20}B_x$ with different boron contents ranging from 6 to 12%. They applied Williamson-Hall and Scherrer's methods to estimate the microstructural parameters (crystal size and microstrain) [6]. In addition, these methods were used to examine and study some other parameters such as lattice strain, microstrain, residual internal stress, dislocation density, number of crystals/cm^2, after determining the correct integral breadth values, β using the integrated amplitude method. Estimated parameters are related to each other [7].

2. Experimental details

2.1. Chemicals and materials

Stoichiometric amounts of pure element of each of Ni (Foil, 99.9 %, Aldrich), Al (Rod, 99.9 %, Johnson) and B (Pieces, 99.8%, Aldrich) were melted under a flow of Argon gas (99.9 %). The pieces of Al and B were usually placed inside a folded foil of Ni and afterward melted either conventionally in an arc-melt furnace or in an induction furnace. The total loss in the samples during synthesis is much smaller than the total weight (typically, on average, 0.5% or less) [1].

2.2. Preparation of the ternary alloys

The arc-furnace is based on the process of low-voltage high-current electric discharge which is used to produce high temperatures that are sufficient-enough to melt most kinds of alloys. A vacuum system is available for pumping the sample space inside the dome to vacuum down to ~10^{-5} torr. After purging three times with pure argon gas (99.9%), a flow of argon is maintained so as to ensure no air entrance. So as to increase sample homogeneity, samples buttons were usually melted several times after being turned around.

2.3. Heat treatments

Different types of heat treatments have been performed to further improve crystallization, phase purity, stress reduction or defect. Quenching processes consist of rapid cooling from a high temperature, ~ 1000°C, to the ambient temperatures by hitting a small piece of the re-melted sample by using a copper hammer in the arc-furnace. The thermal annealing process is carried out by placing the samples in evacuated quartz tubes and then placing the pure argon gas and then leaving the sample in the presence of argon atmosphere at a specified temperature for a certain period of time in a temperature-controlled oven in the computer. After the specified annealing time, samples are usually water-quenched.

2.4. XRD characterization

X-ray diffraction examined at room temperature was recorded of the ternary alloys $Al_3Ni_{20}B_x$ ($0.06 \leq x \leq 0.12$). The Philips X'Pert diffractometer was used to investigate the prepared samples. The diffractometer is equipped with a Cu-Kα wavelength of $\lambda = 0.154184$ nm and operates at 40 kV and 35 mA. Each sample was scanned over $10° < 2\theta < 90°$ to determine any possible formation phases. The continuous scanning method was used, with a slow counting rate of 2^o/min and a small time constant of detector is 2.0 sec. The phase identification was performed by analyzing the positions and intensity of the peaks observed in the diffractogram and comparing them with the database patterns: Powder Diffraction File (PDF) and the International Center of Diffraction Data (ICDD). The properties of the microstructure and the crystal defect parameters in the samples were studied using the line profile analysis (LPA) method according to Lorentzian and Gaussian distributions. As this method has succeeded in estimating the crystallite size and internal microstrain more than other methods, such as SEM or TEM. Because there is a difference between the crystallite size and the particle size or the grain size, where the presence of crystalline blocks or accumulations of multiple crystals to form molecules or grains. In measurement accuracy, the integral breadth was calculated by determining the area under each peak divided by the highest intensity (β =area under the peak/I_o). The observed broadening was investigated by using the step scanning mode with a step size of $2\theta=0.02°$, where the counting time has been kept invariant at five seconds per one step. The broadening corrections were carried out to investigate the crystal defects. The X-ray profile of standard highly crystalline silicon was used to estimate the instrumental broadening corrections.

3. Results and dissections

3.1. XRD analysis

The diffractogram of $Al_3Ni_{20}B_x$ (Fig. 1) correspond to the single-phase character of the face-centered cubic structure. The intensity of the diffraction peaks and how variations in those intensities are related to the chemistry and atomic arrangement or crystal structure of the analyzed material. As shown in the XRD data, the results affirm formation of the single phase of $Al_3Ni_{20}B_x$, the existence of strong diffraction peaks at 2θ values of 23.98, 34.18, 38.38, 42.18, 44.88, 49.13, 51.53, 52.28, 58.28, 77.08 and 78.93^o corresponding to the crystals planes (220), (400), (420), (422), (333), (440), (530), (531), (622), (832) and (752), respectively. In addition to the appearance of many beaks of low XRD intensity and did not show any beaks to indicate the existence of other phases. That is indicating the formation of the single phase and closed matching with the JCPDS card no. 04-0787. Moreover, with the addition of the boron ratio to the Al-Ni alloy, we observed that, a slightly shifted of major plane (333) towards the lower diffracted angle as recorded in Table 2. This indicates that the boron atom with radius (0.796Ǻ) is deposited in the interstitial spaces of the alloy unit cell and therefore a slight displacement occurs in the crystal dimensions and volume of unit cell.

Table 2. *Values of diffraction angles (2θ) of line (333), interplanar spacing (Ǻ), lattice constant (Ǻ) and volume of unit cells ($Ǻ^3$) of $Al_3Ni_{20}B_x$ alloys as function of boron concentrations.*

Parameters	x=6	x=7	x=8	x=9	x=10	x=11	x=12
$2\theta_{(333)}$	44.887	44.773	44.737	44.667	44.537	44.504	44.487
d-values (Å)	2.019	2.024	2.026	2.029	2.034	2.036	2.037
Lattice parameters (Å)	10.493	10.526	10.536	10.542	10.560	10.568	10.579
Volume of unit cell ($Å^3$)	1154.948	1166.346	1169.573	1171.672	1177.651	1180.161	1184.018

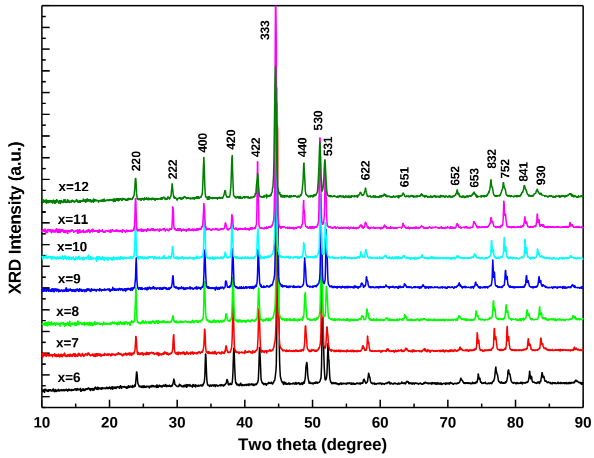

Fig. 1. X-ray diffractograms of Al-Ni-B alloys as a function of B-concentrations.

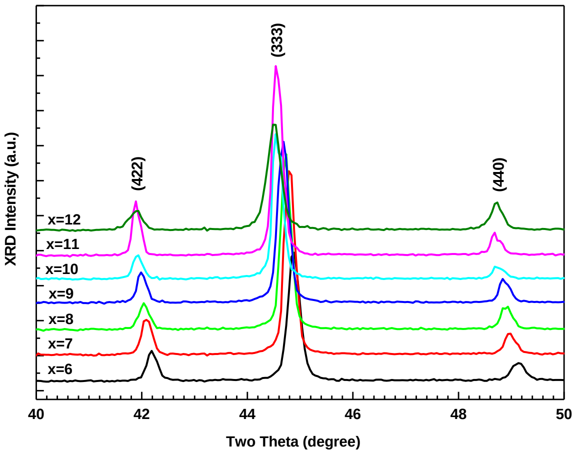

Fig. 2. Illustration of the shift in XRD peaks towards the smallest (2θ) when the B concentration was increased.

The effect of B-concentration upon the diffraction angles, interplanar spacing values (d) and volume of unit cell of the prepared samples of $Al_3Ni_{20}B_x$ alloys were illustrated in Fig. (2) and Table 2. It is obvious that for all diffraction beaks, the d-values were slightly changed with the addition of more boron on the account of Al_3Ni_{20}. This result indicates that; the lattice planes were slightly shifted to upward and the lattice parameter was increases. This is due to the fact that the diameter of the boron atoms (1.592Å) is much smaller than the bond length between the Al-Al and Al-Ni atoms in the unit cell as shown in Table 1. Thus, these vacancies in the unit cell allow the insertion of the boron atoms, which leads to the expansion of the lattice parameters and volume of the unit cell. It was also noted that the amount of increase in the dimensions and volume of the unit cell of the Al-Ni alloys is linear with the increase of the percentage of boron concentration. These results are completely consistent with previous research [8,9]. Moreover, the increasing values of the interplanar distance, d and volume of unit cell may be attributed also to the effect of the internal interface energy or the surfactant of the prepared samples which acts on increasing the surface area of the lattice unit cell of the formed Al-Ni-B alloys samples.

3.2. Lattice parameters

From the XRD analysis of Al-Ni-B alloys should be the crystal structure is face centered cubic structure (fcc). It is confirmed by comparing the peak positions (2θ) of the XRD patterns as a function of boron concentration with the standard JCPDS card no. 04-0787. The lattice constant 'a' for the cubic phase structure is determined by the relation;

$$a = d_{(hkl)}\sqrt{(h^2 + k^2 + l^2)} \tag{1}$$

The calculated values of lattice constants as a function of B-contents are showed in Fig (2) and recorded in Table 2. It can be seen that the changes in the lattice constants are associated with a significantly larger area than non-stoichiometry in relation to boron content (10.4919Å: $Ni_{20}Al_3B_6$; 10.5792Å: $Ni_{20}Al_3B_{12}$). Stadelmaier et al. [10] proposed that the enlargement of the unit cell with higher boron content could be attributed to the replacement of isolated boron atoms with a square antiprismatical coordination by B_2 pairs. This would be very unusual for the structural chemistry of transitional metal borides [11]. In order to illustrate the structure, the chemical causes of the variation in the analysis of the boron content structure based on single-crystal data across the full range of the presence of τ-phase [12] are shown in Table 1. The compositions were derived from the refinement of site occupation factors and corresponded to the corresponding configuration conditions.

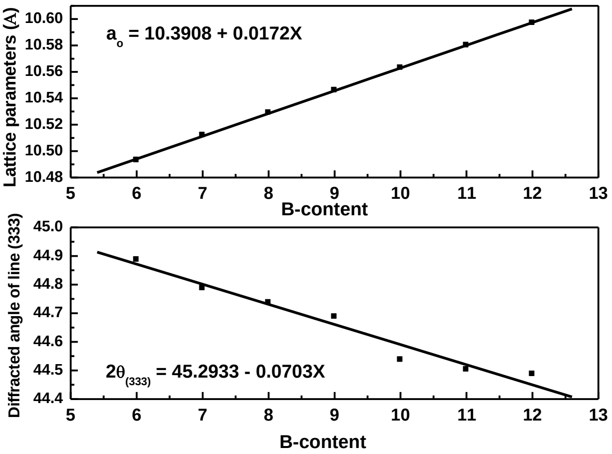

Fig. 3. The lattice parameters and diffracted angle of line (333) as a function of B- content.

From Fig. 3, the values of diffraction angles (2θ) and lattice parameters (a) were found to be changed from 44.290° and 44.284° and from 10.3918Å to 10.3928Å, respectively. These figures were linearly fitted to satisfy the following empirical equations:

$$2\theta_{(333)} = 45.2933\text{-}0.0703X \tag{2}$$

$$a\ (\text{Å}) = 10.3908 - 0.01702\ X \tag{3}$$

where X is the ratio of B-content in the Al_3Ni_{20} compound samples ($0.06 \leq X \leq 0.12$). As is evident, the diffraction angle increased (2θ) but the lattice parameters (a) decreased by increasing the B-content, In general, B ions interstitial in the vacancies between the aluminum and nickel atoms in the crystalline alloys. Therefore, there is an expansion in the dimensions of the unit cell according to the percentage of boron added [1,13]. and this data an agreement with the Vergard's law, the introduction of non-compressible metalloid leads to an isotropic volume expansion [14,15,16].

In addition, with an increase in measurement accuracy, we plotted the Nelson-Riley curve between the calculated lattice parameters (a) for different planes and the error function [17];

$$f(\theta) = \frac{cos^2\theta}{2sin\theta} + \frac{cos^2\theta}{2\theta} \tag{4}$$

A typical Nelson–Riley plot for $Al_3Ni_{20}B_x$ alloys is shown in Fig. 4 and Table 2. It is observed that, the corrected lattice parameters from the Nelson–Riley plots are estimated of 10.570Å . The change in lattice constant for the deformed $Al_3Ni_{20}B_x$ alloy over the bulk clearly suggests that the deformed grains are strained [10].

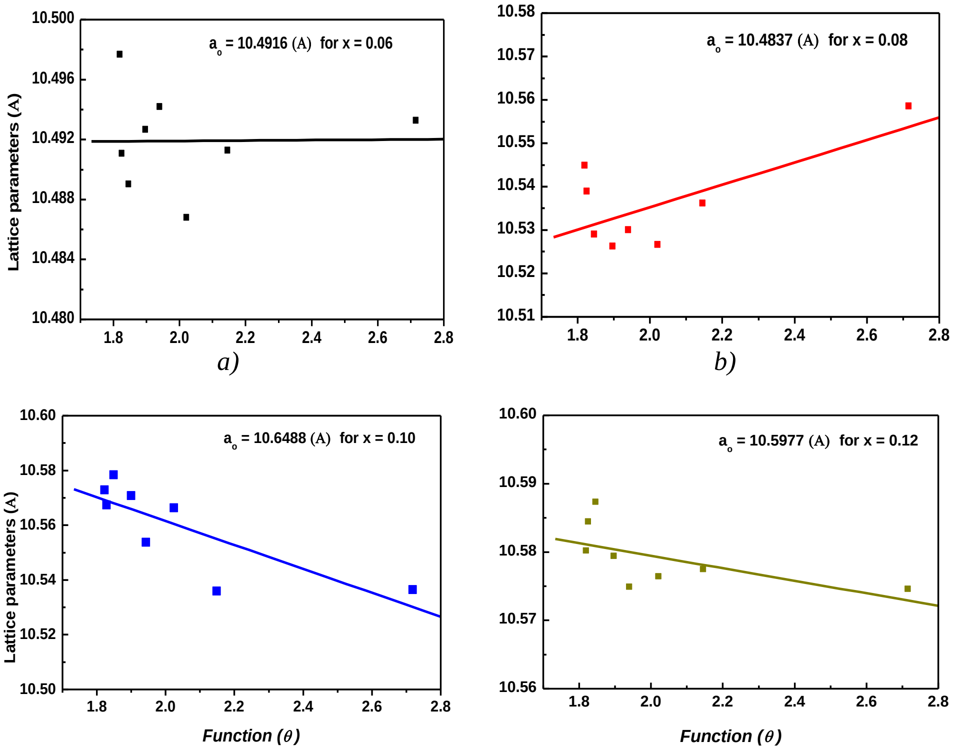

a) b)

c) d)

Fig. 4. Nelson–Riley plot for an $Al_3Ni_{20}B_x$ alloys at different B-contents (a) x=0.06, (b)x= 0.08, (c)x= 0.10 and (d)x=0.12).

From the above data, we can conclude that the structural characteristics of this series are expected to be affected by two properties that are common in this series [11]: the integration of a large number of point defects (such as vacancy or antisite atoms) and large number of interchange points that can occur within different crystalline sites (see Table 1). We evaluated the effect of these two features on the structural properties of $Al_3Ni_{18}B_9$ and $Al_{2.5}Ni_{20.5}B_6$: Figure 2 compares their lattice parameter with that $Al_3Ni_{20}B_x$. It is clear that, the Ni vacancies in the $Al_3Ni_{18}B_9$ do not modify the lattice parameter, the Ni substitution of Al atoms in $Al_{2.5}Ni_{20.5}B_6$ causes a significant reduction in the lattice parameter. These conclusions highlight the importance of Al-atoms in determining the dimension of the unit cell.

3.3. Microstructural parameters analysis

3.3.1. Crystallite size and microstrain determinations

The size of crystals and microstrain plays a crucial role in the behavior of the material and its physical properties, especially the microstructural properties. Their importance is due to their specific characteristics and potential uses in advanced technological applications. The x-ray diffraction line profile analysis is considered to be one of the most accurate techniques to determine the crystallite size [18-20] and the non-uniform displacements strain of atoms in relation to their reference lattice positions [21]. The shape of the line caused by lattice distortions in crystallization, which revealed that the broadening of the diffraction peak with *hkl* indices. The Williamson-Hall's method is the preferred method to be used in the case of samples containing several x-ray diffractions peaks, as in the current samples. The integral breadth values (the area under the peak/maximum intensity of peak) of the characterized peaks were measured. The observed integral breadth (B) in the sample is corrected for instrumental broadening (b) to give corrected integral breadth (β) using the following relationship [22].

$$\beta = B - \left(\frac{b^2}{B}\right) \tag{5}$$

This correction assumes that the peak shape is somewhat between Gaussian and Cauchy (Lorentzian) distributions which results in more accurate results. Depending on the different positions, the separation between the crystallite size (D) and microstrain $< \varepsilon >$ broadening analysis are performed using the Williamson and Hall (W-H) method. One of the most important sources of line broadening is three sources the instrumental, crystallite size and strain broadening. To do an accurate analysis for size and/or strain effects one must accurately account for instrumental broadening using a high crystalline sample. The manner of doing this differs depending upon the peak shape. The equation of this method is given in the following equation [23- 26]:

Lorentzian Distributions

$$\beta_{hkl} = \beta_{strain} + \beta_{crystallite\ size} + \beta_{inst} \tag{6}$$

$$\beta_{correct} = (\beta_{hkl} - \beta_{inst}) = \beta_{strain} + \beta_{crystallite\ size} \tag{7}$$

Gaussian Distributions

$$\beta^2_{hkl} = \beta^2_{strain} + \beta^2_{crystallite\ size} + \beta^2_{inst} \tag{8}$$

$$\beta^2_{correct} = (\beta^2_{hkl} - \beta^2_{inst}) = \beta^2_{strain} + \beta^2_{crystallite\ size} \tag{9}$$

According to Williamson and Hall (W-H) method, we can write the total broadening equation in the beaks as follows;

$$\beta_{correct} = \left(\frac{k\lambda}{D cos\theta}\right) + 4\langle\varepsilon\rangle \tan\theta \tag{10}$$

Rearrangement equation (10) gives

$$\beta_{correct} cos\theta = \frac{k\lambda}{D} + 4 < \varepsilon > sin\theta \tag{11}$$

$$\beta^2_{correct} cos^2\theta = (\frac{k\lambda}{D})^2 + 16 < \varepsilon^2 > sin^2\theta \tag{12}$$

where $\beta_{correct}$ and $\beta^2_{correct}$ are the pure broadening of the sample (expressed in radians), θ is the diffraction angle, k is the shape factor and in our case it is equal 0.94. The incident X-ray wavelength λ is ($\lambda = 0.154184$ nm), D is the crystallite size and $< \varepsilon >$ is the average microstrain.

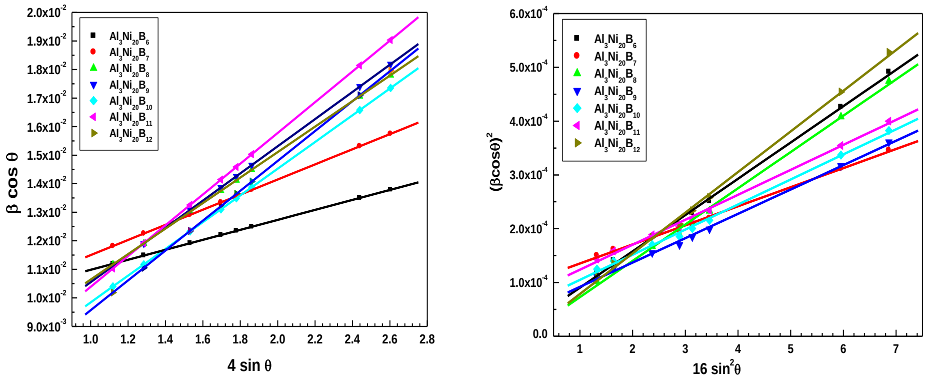

a) *b)*

Fig. 5. (a) Williamson–Hall plots of (β cosθ) and (4 sinθ) of Al_3Ni_{20} alloys for different B-contents; (b) Williamson–Hall plots of $(β\ cosθ)^2$ and $(16\ sinθ\ )^2$ of Al_3Ni_{20} alloys for different B-contents.

From the linear fitting of the W–H plots at different boron content of the Al_3Ni_{20} alloys (Fig. 5 a & b), it has been confirmed that the X-ray line broadening in polycrystalline material is due to the presence of crystallite size effect as well as microstrain effect. The slopes of the W–H plot represent average internal microstrain in the Al_3Ni_{20} alloys while the inverse of the intercept at (β cosθ/λ) and $(β\ cosθ/λ)^2$ axis gives the crystallite size according to the Lorentzian and Gaussian distributions. Figure (6a) shows the dependence values for the average crystalline size determined from W-H on the contents of the boron, which was seen as a linear increase. On the other hand, the microstrain demonstrated the behavior of the variance, i.e. gradually decreasing with increasing the contents of B, as shown in Figure (6b). This difference may be due to increased demand (preferred orientation degree) and increased structural defects including grain boundaries. Also, it has been quantified by analyzing line profile. Because of the high degree of preferred orientation, one arrangement of meditation can be measured with sufficient accuracy.

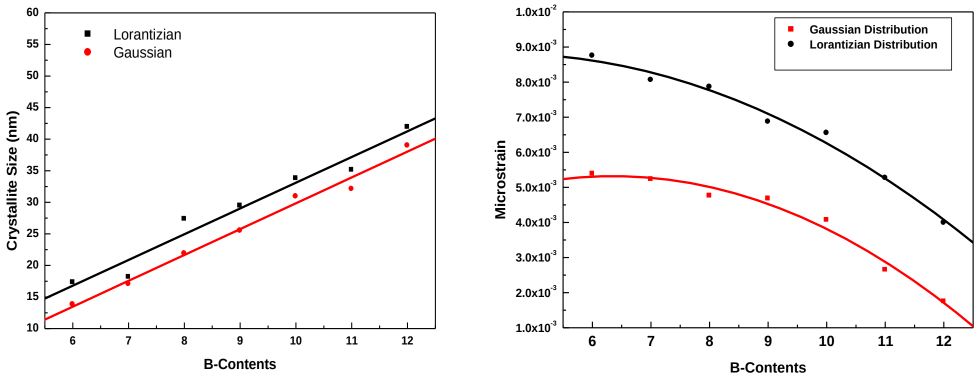

a) *b)*

Fig. 6. (a) Shows the dependence values for the average crystalline size as a function of B-concentration; (b) Shows the dependence values for the microstrain as a function of B-concentration.

3.3.2. Residual internal stress

The principles of internal stress analysis by X-ray diffraction are based on the measurement of angular lattice strain distributions. Residual internal stress is the stress that remains in the material after removing the external force that caused the stress. Total internal stress consists of three types of stress. They are thermal stress, mechanical stress and an intrinsic stress. Thermal stress depends on the coefficient of thermal expansion, but the intrinsic stress is due to the accumulation of crystalline defects, and these defects are built into the alloys of the Al-Ni-B during the compresses. On the other hand, mechanical stress is due to the deformation effect and elastic parameters of Al-Ni-B alloys. To get rid of the thermal stress, the samples were annealing, which was found at 5.00% of total stress. Therefore, it is believed that for high melting materials like Ni, internal stress accumulates and tends to dominate over thermal stress. The following relationship calculates the average internal stress in the prepared samples [27],

$$S = \frac{Y}{2\gamma}\left(\frac{a_o - a}{a_o}\right) \tag{13}$$

where (*Y*) and (γ)) are Young's modulus and Poisson's ratio of the Al-Ni-B alloys, respectively. The calculated values of (*Y)* and (γ) were found to be approximately 1.12 $x10^{11}$Pa and 0.33, respectively [28,29], while (***a₀***) is the bulk lattice constant of Al-Ni-B alloys (Ref. PDF number 04-0787). The estimated value of *(a*) refers to the lattice constant that is perpendicular to the original plane. The origin of the internal stress is also related to the lattice misfits who is turn depend upon the deformation degrees. Calculated values for internal stresses of Al-Ni-B alloys with different B-concentration in Table 3 and Fig. 7.

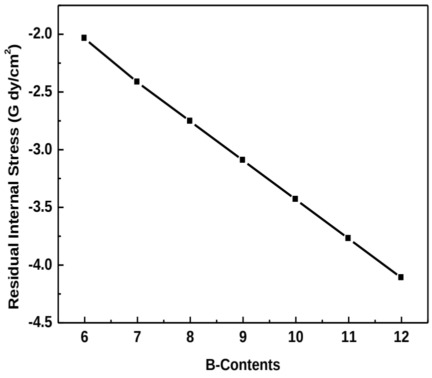

Fig. 7. Residual internal stress as a function of boron concentration in Al-Ni alloys.

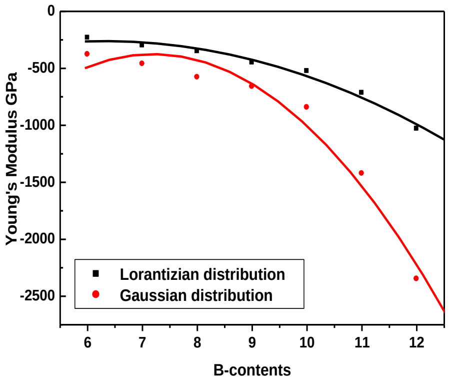

Fig. 8. Calculated Young's modulus as a function of boron concentration in Al-Ni-B alloys.

***Table 3**. The obtained values of the crystallite size (D), the average microstrain <ε>, Young's modulus, $E_{(hkl)}$, the residual internal stresses (σ) and the dislocation density (δ).*

Samples	D_L (nm)	D_G (nm)	$<\varepsilon>_L$ $\times 10^{-4}$	$<\varepsilon>_G$ $\times 10^{-4}$	$E_{(hkl)}$ GPa.	$(\sigma)\times 10^{9}$ (dy/cm^2)	$(\delta)_L \times 10^{15}$ $Line/m^2$	$(\delta)_G. \times 10^{15}$ $Line/m^2$
$Al_3Ni_{20}B_6$	17.32	13.81	87.50	53.90	*-232.84*	*-2.04*	*7.17*	*5.54*
$Al_3Ni_{20}B_7$	18.17	17.06	80.60	52.30	*-299.77*	*-2.42*	*6.30*	*4.35*
$Al_3Ni_{20}B_8$	27.36	21.89	78.60	47.60	*-350.52*	*-2.76*	*4.08*	*3.09*
$Al_3Ni_{20}B_9$	29.47	25.50	68.70	46.80	*-450.36*	*-3.09*	*3.31*	*2.60*
$Al_3Ni_{20}B_{10}$	33.80	30.93	65.50	44.70	*-524.09*	*-3.43*	*2.75*	*1.87*
$Al_3Ni_{20}B_{11}$	35.12	32.10	62.70	26.50	*-715.70*	*-3.77*	*2.13*	*1.17*
$Al_3Ni_{20}B_{12}$	41.92	38.98	59.90	17.50	*-1030.24*	*-4.11*	*1.35*	*0.64*

Clearly, internal stress values (σ) were found in the range ($-2.04\text{x}10^9$) and ($-4.11\text{x}10^9$) dy/cm^2, negative values indicate the compression state. Also, a linear relationship was observed between the concentration of boron and the absolute value of internal stress. This is because the clamping constant of the prepared samples is greater than the value of the dislocation while (Y) and (γ) are almost unchanged. This is the agreement with the announced results [30, 31]. Thus, the Young's modulus value for each individual XRD line (the eight major lines) was calculated according to Equation (14) and the mean value of $E_{(hkl)}$ for each $Al_3Ni_{20}B_x$ sample was taken and included in Table 3. The calculated values of the Young's modulus were roughly identical to those calculated for the bulk Al-Ni alloys [32,33]. Thus, the residual internal stress value (σ) can be determined. The mean values of the remaining internal stresses were calculated according to this simple known equation.

$$(E_{(hkl)}) = \frac{Internal\ residual\ stress}{average\ microstrain} = \frac{\sigma}{<\varepsilon>}, \quad \sigma = <\varepsilon> E_{(hkl)} \tag{14}$$

The calculated values of the Young's modulus are recorded in Table 3 and are represented in Fig. 8. Note that the Young's modulus values decreased when boron content was increased. This finding may be attributed to the fact that the free volumes at the grain boundary were reduced by the small crystal agglomeration and the incorporating of the structural units with each other. Where B increases the increase in the agglomeration of the crystallite sizes. At the same time, the volume of unit cell decreased with the increase of B ratio and therefore vacancies also decreased. This in turn increases the surface area of the particle size, thus reducing the estimated residual stress values [34].

3.3.3. Lattice strain estimation

The strain is the term used to express the distortion that occurs in the dimensions of the physical sample relative to the original length. There are two types of strain, namely, uniform and non-uniform strains. The regular strain causes an expansion or contraction of the unit cell in an isotropic way [33]. This leads to some changes in the lattice parameters of the unit cell, thus causing a shift in the observed peaks, but does not cause a peak broadening. While the irregular strain leads to regular shifts of atoms from their original locations and thus leads to peak broadening [34]. The irregular strain arises due to the presence of many defects within the material, such as point defects, plastic deformation and poor crystallization of the material. The strain observed in the current $Al_3Ni_{20}B_x$ samples was an irregular strain, which caused the XRD peaks to shift from their original positions as well as to broadening them. This strain ($\Delta a/a_o$) is sometimes called lattice strains or relative changes in lattice constants. The lattice strain of the current $Al_3Ni_{20}B_x$ samples was found to be a non-uniform strain, causing the shift to XRD peaks from their original positions.

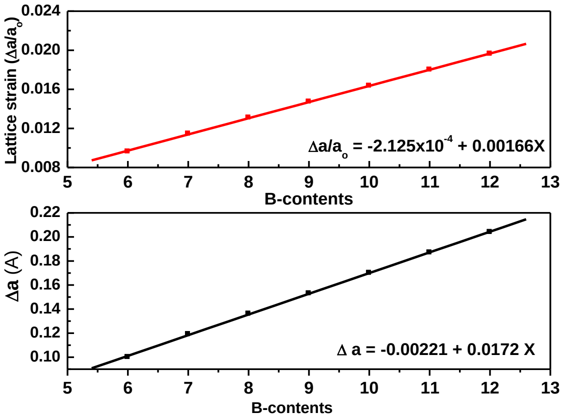

Fig. 9. The change of lattice parameter (Δa) and lattice strain ($\Delta a/a_o$) as a function of boron concentration in Al-Ni-B alloys.

The calculated values of the change in lattice parameters and the lattice strains were represented in Figure (9). It can be easily observed that the behavior of these changes was linear with concentration B in the Al-Ni-B alloys. This is due to changes in the unit cell constant in all directions.

3.3.4. Dislocation density

Density of dislocation is defined as the length of dislocation lines per unit volume. This is due to the defect of crystal associated with mis registry in the lattice. Unlike vacant positions and interstitial atoms, dislocations are not equilibrium imperfections, i.e. thermodynamic considerations are insufficient to account for their presence in observable densities. In fact, the mechanism of growth involving dislocation is an important in matter. The intensity of dislocation was estimated using the Williamson and Smallman method using the relationship [35,36].

$$\rho = \frac{15\varepsilon}{aD} \tag{15}$$

The calculated values of dislocation density for Al-Ni-B alloys as a function of B concentration in Al-Ni-B alloys are recorded in Table 4 and shown in Fig. 10.

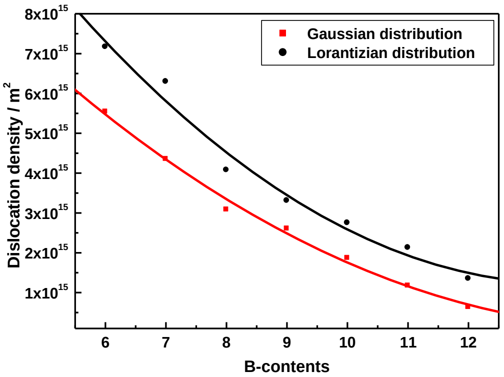

Fig. 10. The dislocation density per unit area as a function of B-concentration as a function of Al-Ni-B alloys.

It is clear that the dislocation density decreased with the increase of B content in the Al-Ni-B alloys. The decreasing value of the dislocation density can be attributed to improved crystallization of samples by adding more concentration of boron and diminishing of the free volumes and vacancies [22].

4. Conclusion

Stoichiometric amounts of $Al_3Ni_{20}B_x$ (0.06<x>0.12) phases using pure Ni (99.9%), Al (99.9%), and B (99.8%) elements were melted under argon atmosphere (99.9%) in conventional arc-melt or induction furnaces. The crystallography, microstructure and crystal imperfections of samples were studied and investigated. Adding B element leads to increase the crystallization of samples, in addition it caused a little shift of for the X-ray diffraction lines towards the larger angles. XRD-Line profile analysis by Lorentzian and Gaussian distributions were used to estimate the pure broadening of samples. Williamson-Hall method was used to get the crystallite size and microstrain. The estimated values of crystallite size increased with the increasing of B-content. Both the microstrain and lattice strain decreased with increasing the B element.

These results were ascribed to the diminishing of the free volumes and the vacancies which existed between the grain boundaries. The internal residual stresses, the dislocation density of the Al-Ni-B samples were estimated and studies as functions of the B- ratio. Generally, all the crystal defects were found to be decreased with increasing the B-content of the $Al_3Ni_{20}B_x$. This means that the doping of B element leads to the improvement of the microstructural characterization. In addition, the crystallite size was increased as adding more of B element due to the agglomerating of the small crystallites and diminished the free volumes at the boundaries, which support the results that obtained from XRD. From these measurement, the crystallization of $Al_3Ni_{20}B_x$ alloys is optimum at concentration of B percentage of 11%.

References

[1] M. Elhadi, M. ElMassalami, H. Takeya, R.E. Rapp, F.A.B. Chaves, A. Elzubair, J. of Alloys and Compounds **499**, 11 (2010).
[2] A. Urrutia, S. Tumminello, D. G. Lamas, S.Sommadossi; Procedia Materials Science **8**, 1150 (2015).
[3] H. Hillebrecht, M. Ade, Angew. Chem. Int. Ed. **37**, 935 (1998).
[4] H. Choe, D. C. Dunand, Acta Materialia **52**, 1283 (2004).
[5] H. A. Hafez, M. M. Faeag, Journal of material science **16**, 1223 (1981).
[6] R. H. Jones, C. H. Henager, P. P. Trzaskoma, N. S. Stoloff, T. S. Moffat, B. D. J. Lichter, Metals, 18 (1988).
[7] K. Aoki, O. Izumi, J. Mat. Sci. **14**, 1800 (1979).
[8] M. Khairy, M. A. Mousa, Journal of Ovonic Research; Vol. 15, No. 3, (2019)181 – 198
[9]S. Satheeskumar, V. Jeevanantham, D. Tamilselvi, Journal of Ovonic Research; Vol. 14, No. 1, (2018) 9 – 15
[10] H. H. Stadelmaier, H. H. Davis, H. K. Manaktala, E.-T. Henig, Z. Metallkde. **80**, 370 (1989).
[11] H. H. Stadelmaier, A. C. Fraker, Metall. **16**, 212 (1962).
[12] H. H. Stadelmaier, R. A. Draughan, G. Hofer, Z. Metallkde. **54**, 640 (1963).
[13] M. S. F. Lima, P. I. Ferreira, Intermetallics **4**, 85 (1996).
[14] A. H. Eid, M. B. Seddek, A. M. Salem, T. M. Dahy, Vacuum **83**, 401 (2009).
[15] L. Vegard, Zeitschrift für Physik **5**(1), 17 (1921).
[16] Z. Nourbakhsh, J. Alloys Compounds **505**, 698 (2010).
[17] Z. Zhang, C. Zhong, Y. Deng, L. Liu, Y. Wu, W. Hu, RSC Adv. **3**, 6763 (2013).
[18] A. Chen, G. Yang, H. Long, P. Lu, W. Zhang, H. Wang, Mater. Lett. **91**, 319 (2013).
[19] S. Eisermann, A. Kronenberger, A. Laufer, J. Bieber, G. Haas, S. Lautenschlager, G. Homm, P. J. Klar, B. K. Meyer, Phys. Status Solidi A **209**, 531 (2012).
[20] A. Musa, T. Akomolafe, M. Carter, Sol. Energy Mater. Sol. Cells **51**, 305 (1998).
[21] Alaa A. Akl, A. S. Hassanien, Superlattices and Microstructures **85**, 67 (2015).

[22] Y. T. Prabhu, K. V. Rao, V. S. S. Kumar, B. S. Kumari, J. of Nano Science and Engineering **4**, 21 (2014).
[23] A. H. Eid, M. B. Seddek, A. M. Salem, T. M. Dahy, Vacuum **83**, 401 (2009).
[24] L. Vegard, Zeitschriftfür Physik **5**(1), 17 (1921).
[25] B. E. Warren, X-ray Diffraction, Addison Wesly Publishing, Co., London, 18 (1969).
[26] B. D. Cullity, Elements of X-ray Diffraction. Addison-Wesley Publishing Company Inc., California, 1956.
[27] A. S. Hassanien, A. A. Akl, Phys. B **473**, 11 (2015).
[28] E. Cesari, C. Segui, J. Pons, F. Perell, Journal de Physique **111**(6), 1996.
[29] A. S. Hassanien, A. A. Akl, J. Alloys Compd. **648**, 280 (2015).
[30] R. J. Ong, D. A. Payne, N. R. Sottos, J. Am. Ceram. Soc. **88**, 2839 (2005).
[31] R. Yogamalar, R. Srinivasan, A. Vinu, K. Ariga, A. C. Bose, Solid State Communications 149, 1919 (2009).
[32] M. J. Weber, Handbook of Optical Materials, CRC Press, London, 2003.
[33] M. E. Fitzpatrick, A. T. Fry, P. Holdway, F. A. Kandil, J. Shackleton, L. Suominen, Measurement Good Practice Guide No. 52, National Physical Laboratory, 2005.
[34] S. Adachi, Handbook on Physical Properties of Semiconductors, Springer, 2004.
[35] C. S. Barret, T. B. Massalski, Structure of Metals, Pergamon Press, Oxford, 1980.
[36] S. Ilican, Y. Caglar, M. Caglar, J. Optoelectron. Adv. M. **10**, 2578 (2008).